High photoelectrochemical activity and stability of Au-WS$_2$/Silicon heterojunction photocathode

Longhui Zeng,[a] Yang Liu,[a] Shenghuang Lin,[a] Wayesh Qarony,[a] Lili Tao,[a] Yang Chai,[a] Xuming Zhang,[a] Shu Ping Lau,[a] Yuen Hong Tsang*[a]

The first two authors contributed equally to this work

[a] Department of Applied Physics and Materials Research Center, The Hong Kong Polytechnic University, Hung Hom, Kowloon, Hong Kong, 99077, China

* Corresponding author. E-mail: Yuen.Tsang@polyu.edu.hk

Abstract: Although silicon has been widely employed as light harvesting antenna in photocatalysts due to its cost advantage, it suffers from low efficiency and poor stability due to photocorrosion of Si. To overcome this problem, a heterojunction photocathode was produced by coating a WS$_2$ thin-film on *p*-type Si. Our proposed method can further improve the photocatalytic activity and stability. The homogeneous WS$_2$ films with large surface area and tens-of-nanometers in thickness were prepared through magnetron and post-annealing process. This film not only functions as a protective layer to isolate the Si from the harsh electrochemical environment, but also forms a junction at the interface between WS$_2$ and *p*-type Si to facilitate the charge separation and transport processes. Additionally, further enhancement of visible photocatalytic performance was achieved by depositing Au film on WS$_2$/*p*-Si through thermal evaporation and the highest value of the photocurrent intensity achieved is up to ∼ 4.5 μA/cm^2 at 0 V versus Ag/AgCl. Besides, photoelectrochemical instability of WS$_2$/*p*-Si electrodes can be minimized by adding Au coating. Our results suggest that adding the Au-WS$_2$ on *p*-Si can benefit carrier separation and providing physical protection of the Si layer. Therefore, it can further improve the overall photocatalytic activity and stability.

Keywords: WS$_2$; WS$_2$/Si; heterojunction; photocathode; photocatalyst

1.Introduction

The global energy crisis and many environmental problems could potentially be solved provided that photoelectrochemical (PEC) water splitting can be done in a cost effective way with high efficiency. PEC water splitting is a promising approach to generate clean and renewable energy source-hydrogen (H_2) and oxygen (O_2) by using solar energy. This research topic has gained extensive and increasing interests. The research works for searching for low cost, efficient and durable photoelectrode are particularly popular. Therefore, some common semiconductors such as Si, III-V, and II-VI have been extensively studied previously. Among these materials, silicon has attracted considerable attention due to its favorable properties and it has been widely applied in various fields such as electronics, [1, 2] thermoelectric,[3] solar cell,[4] and photo-electrochemical water splitting.[5, 6, 7] At room temperature, silicon with bandgap of 1.12 eV is considered to be one of the most promising candidates for photocathode because of efficient solar energy harvesting across the entire solar spectrum, low material cost and abundance (> 90% in the Earth's crust).[8] For these reasons, silicon-based photoelectrodes and photocatalysts have been widely developed for solar energy harvesting and conversion. However, the poor photoelectrochemical stability is one of the key problems for the development of high performance Si-based photocatalysts as Si is thermodynamically vulnerable to photoactive dissolution, or photocorrosion.[9] In order to develop effective approaches to stabilize the photoactivity of Si, expensive metal and rare earth metals e.g. Pt,[10] Ir/IrOx [11] were used for performance and stability enhancement preiously. Searching for the alternative low-cost and scalable strategies to solve stability issue is still an on-going and hot research topic with in the field.

Recently, the emergence of layered two-dimensional transition-metal disulfides (2D TMDs) has garnered much attention due to their favorable electrical and optical properties for fiber

laser,[12] photodetector,[13] photocatalyst.[14] It is noated that 2D TMDs such as MoS_2, SnS_2, TiS_2, WS_2, $MoSe_2$, WSe_2 are emergying as important class of 2D materials in photocatalysis applications. By virtue of their potential use as electrodes for photocatalysts, TMDs are low cost and earth abundant and they can serve as promising materials to replace the more expensive Pt, Rh, and Ir suggested in the previous study. It has been reported that WS_2 and MoS_2 with suitable bandgaps (1.1-1.7 eV) matched well with the solar spectrum and possess high densities of active edge sites for photocatalysis. [15, 16] Actually, WS_2 shows high thermal stability and wide operational temperature range as lubricants.[17] Moreover, WS_2 has excellent chemical stability and can serve as protecting barrier to prevent photocorrosion of Si. Furthermore, WS_2 could form a WS_2/p-Si heterojunction for performance enhancement of photocatalytic applications. It has been known that the induced electrical field between the WS_2 and Si could be very strong due to the difference in work function,[15] which could facilitate the transport of the photo-generated electrons from Si to WS_2 and then to the electrolyte/solid interface.

Preparation of uniform and large area WS_2 thin film is one of the most important steps for high-quality device fabrication. However, WS_2 films reported in recent papers are usually acquired by exfoliation, solution-based syntheses, and chemical vapor deposition (CVD).[13, 18] In fact, it is difficult to control the uniformity of size and thickness and deposited into a thin film by using those WS_2 flakes fabricated by mechanical or chemical exfoliation.[19] Uniform and ultrathin WS_2 layers can be synthesized on oxide substrates by using CVD method, but the surface of CVD-grown WS_2 layers contains mainly electrochemically inactive basal planes.[14] The magnetron sputtering deposition method has some advantages over the CVD method including simplicity, low cost, high production speed and scalability. Therefore, to overcome these problems, direct magnetron sputtering deposition is employed to fabricate WS_2/p-type semiconductor heterojunctions.

In this study, a facile and simple method to functionalize Si photocathode with WS_2 thin films is reported. To further boost the device performance, Au film was coated on WS_2 to collect the electrons for high efficient photocurrent conduction. The as-prepared Au-WS_2/p-Si photocathode exhibited enhanced photo-activity with much higher photocurrent stability. The excellent performance of Au-WS_2/p-Si can not only offer strong potential for application of silicon-based photocatalysts/photoelectrodes for solar energy harvesting but also provide new insights for enhancing and stabilizing other photocatalytic systems.

2. Experimental Section

WS$_2$ Film Deposition: WS_2 films on the p-Si substrate were produced by magnetron sputtering method. The WS_2 precursor film was first deposited on the clean p-Si substrate through sputtering by using sintered WS_2 target. The radio frequency (RF) power density, argon gas pressure, and substrate temperature were set to be 2.96 W/cm^2, 5 mTorr, and 200 °C, respectively; and deposition time of 5 mins. To improve the film crystallinity, the as-prepared WS_2 films were annealed in Ar atmosphere at 800 °C and kept stable for 2 hours.

Device Fabrication: To fabricate the Au-WS_2/p-Si photocathode, p-type (100) Si (resistivity 1−10 Ωcm) substrates were ultrasonically cleaned in alcohol, acetone and deionized water in sequence, and dried under a stream of nitrogen gas. WS_2 film was deposited under the conditions mentioned above. Afterward, Au (50 nm) films were deposited onto the WS_2 film by thermal evaporation.

Characterizations of Materials and Devices: UV-Vis absorbance and transmittance spectra were measured by a SHIMADZU UV-2550 UV-Vis spectrophotometer. The Raman spectra were carried out on an HR-800 Raman spectrometer with a 488 nm argon ion laser. The X-ray diffraction (XRD) pattern was recorded using a RigakuSmartLab X-ray diffractometer. The surface morphology and height profile of samples were obtained by atomic force microscopy (AFM, VeecoNanoscope V). The morphology, crystal structure, and chemical composition

were investigated using a field emission transmission electron microscope (FETEM, JEOL Model JEM-2100F), equipped with an energy dispersive spectrometer (EDS). Additionally, the photocatalytic reaction was measured with an electrochemical workstation (CH Instruments, CHI 660E) in a stand and three-electrodes configuration under a 300 W Xe lamp with a UV-cutoff filter to obtain visible light with $\lambda \geq 420$ nm.

3. Results and Discussion

Figure 1a illustrates the optical absorbance and transmittance spectra of the post-annealed WS$_2$ films on quartz. The film size is 2 cm × 2 cm on quartz (inset in Figure 1 a). In general, WS$_2$ films exhibit high optical transmittance in the near infrared wavelength region, while it shows relatively strong photo-absorption in the visible range. Therefore, the WS$_2$ film possesses considerable photo-absorption covering the entire UV-Visible range of 200-900 nm, which is desirable for solar energy harvesting of photocatalyst. [20] Considering the characteristic of an indirect bandgap semiconductor, the optical bandgap of WS$_2$ film was calculated by using the Tauc plot method *via* the relationship $\alpha h v \propto (h v - E_g)^{1/2}$. A plot of $(\alpha h v)^{1/2}$ *versus* the energy of absorbed light can be converted according to the Kubelka-Munk function of the UV-Vis spectrum, which is expressed in Figure 1b. [21, 22] The bandgap of WS$_2$ film estimated from the intercept of the tangent to the plot is 1.262 eV closed to the value reported before,[23] thus suggesting that the photocatalyst can be activated by NIR light. The PL and Raman spectra are typically utilized to analyze the optical property and crystal structures. As shown in Figure 1c, the PL of the as-grown sample was measured by confocal PL spectroscopy, exhibiting a strong peak located at ~984 nm (corresponding to ~1.26 eV), which is in good agreement with our calculated bandgap of WS$_2$. The Raman spectra shown in Figure 1d indicates there is a great difference between the scattering modes of Raman spectra for WS$_2$ nanosheets with different layers. It is obvious that WS$_2$ nanosheets show two strong signals from in-plane E^1_{2g} and out-of-plane A_{1g} vibrations. In addition, peaks belonging

to E^1_{2g} and A_{1g} are located at 354.7 and 419.9 cm^{-1}, respectively. The frequency difference of the two Raman peaks of the WS$_2$ film is 65.2 cm^{-1}, indicating a multilayer of WS$_2$.[24, 25]

To quantify the WS$_2$ film thickness, atomic force microscopy (AFM) height profile measurements across the edge of an as-grown WS$_2$ was performed and shown in Figure 2a. The average height of the film measured from underlying SiO$_2$/Si substrate surface corresponds to ~27.2 nm. Further investigation of the crystalline structure and the composition of the WS$_2$ and Au-WS$_2$ films, X-ray diffraction (XRD) analysis were carried out. As observed from the measured XRD patterns shown in Figure 2c, three diffraction peaks located at 14.42°, 28.98°, 44.06°, corresponding to the (002), (004), (006) crystal planes of hexagonal WS$_2$, respectively. [26] Additionally, after the decoration of Au film, another new XRD peak appeared at 2θ of 38.3°, which can be identified as the characteristic peak of (111) crystal planes of Au.[16, 27]

The microstructure of the film was viewed by using transmission electron microscopy (TEM) or High-Resolution Transmission Electron Microscopy (HRTEM) as depicted in Figure 3. Figure 3a shows the typical HRTEM images of WS$_2$, disclosing that the WS$_2$ film is polycrystalline with horizontally grown nanosheets and vertically standing layered structure. Figure 3b gives the HRTEM image of the vertically grown WS$_2$ nanosheets, showing the 0.625 nm interlayer distance of WS$_2$, can be indexed to the (002) plane of hexagonal WS$_2$. [16] The horizontal layer distance of ≈ 0.27 nm in the HRTEM image of Figure 3c corresponds to the (110) planes, which is in good agreement with reported results.[13, 28] To get more information about the growth mechanism of WS$_2$ and structure of the WS$_2$/Si heterojunction, the cross-sectional TEM views of the sample were measured and shown in Figure 3d-e. From Figure 3d, the WS$_2$ film deposited by sputtering has a uniform thickness of approximately 30 nm, which is closely consistent with results shown in AFM image of Figure 2b. Interestingly, the growth direction of the WS$_2$ film was changed from horizontal to vertically aligned layers, while the deposition time of sputtering increases and then results in more exposed vertical

growth active edge sites.[29] Recent reports demonstrated that TMDs with more vertically aligned structure have more catalytic active sites for higher catalytic activity.[30, 31, 32] From the high-resolution TEM image at the junction interface (Figure 3e), we can see that a thin SiO_2 interfacial layer ($\approx$ 10 nm) was found between Si substrate and the WS_2 film. The thin SiO_2 layer is mainly caused by oxidation of Si during film deposition under exposure of the residual oxygen in the chamber. The presence of tungsten (W) and sulphur (S) elements are contained in the prepared sample, corresponding resolved peaks in Figure 3f.

The WS_2 thin films were deposited on a clean p-type Si substrate by magnetron sputtering. The Figure 4a shows the current-voltage (I-V) curves of a typical n-WS_2/p-Si device at room temperature, from which we can see that the device exhibits obvious rectification due to the presence of a barrier between WS_2 and Si. The schematic of n-WS_2/p-Si heterostructure was shown in the inset of Figure 4a. This obvious rectification characteristic can be understood from the energy band diagram illustrated in Figure 4 (b). Once the WS_2 films were deposited on Si wafer, partial carriers in WS_2 tend to move to the Si side and consequently energy levels near the WS_2 surface will bend upward, and energy levels near the Si surface will bend downward, leading to the formation of the built-in electric field near WS_2/Si interface. The rectification characteristic is formed as a result of the energy difference between the Fermi level of WS_2 and the Si. Under the light illumination, the photogenerated electron-hole pairs are separated by the built-in electric field. The resulted free electrons and holes will move towards opposite directions, giving rise to a generation of photocurrent in external circuit.[33] In order to verify this point, photoelectrochemical (PEC) measurements with the fabricated photocathodes devices were performed using a standard three-electrode cell with an electrolyte of 0.5M H_2SO_4. Figure 5a shows a schematic drawing of the PEC measurement setup. Samples are used as photocathode and the counter electrode is Pt. The electrons-holes pairs were generated when device photocathodes were irradiated. The electrons were then promptly transferred from Si to WS_2 and conduct through the Au film, and then H^+ was

reduced by the electrons on the Au film surface to generate H_2. On the other hand, the remaining holes will oxide OH^- in the water to generate O_2. According to this PEC setup, the time course photocurrent response of sample electrodes under chopped visible light illumination is depicted in Figure 5b-c. The photocurrent density of pure silicon substrate was measured as low as 0.07 $\mu A/cm^2$ at zero bias *versus* Ag/AgCl, of which the photoelectrical activity is relatively poor. We believe that the poor photoelecrical activity is attributed to the native oxide of Si substrate (see Figure 3 e), which will impede electron-hole pairs seperation and transportation. However, the photocurrent of WS_2/p-Si was about 1.1 $\mu A/cm^2$ from the sample fabricated with heterojunction between WS_2 and Si. In other words, the photocurrent density of the WS_2/p-Si heterojunction improved up to approximate 16 times higher than that of the pristine Si photocathode. After the incorporation of Au film on WS_2, the corresponding photocurrent was significantly increased to 4.5 $\mu A/cm^2$ under same conditions, which is more than 4 times higher than that of WS_2/p-Si. It is confirmed that the presence of Au film can greatly increase the photocatalytic activity. The photocurrent of our devices under reverse bias was also measured. Figure 5c shows the chopped cathodic photocurrents of Si, WS_2/p-Si, and Au-WS_2/p-Si at the fixed potential of -1V vs. Ag/AgCl. It also clearly shows the photorcurrent of Au-WS_2/p-Si is the highest (-0.37 mA/cm^2) among the three samples. Table 1 summarizes the key results of our sample with previous TMDs.[34, 35, 36, 37] Therefore, it can be concluded that the increased photocurrent is attributed to more efficient electron injection from Si to WS_2, and the presence of Au film serving as a good electron acceptor and thus it reduces the charge recombination rate.[21, 38] This conclusion can be further confirmed by the results of EIS.

As shown in Figure 6 (a), the arch of Au-WS_2/Si was much smaller than that of bare Si and WS_2/Si, implying that it can significantly reduce the resistance of the charge movement at the interface by adding the WS_2 and Au film and smaller arc radius implies a much higher efficient charge transfer.[39] Another objective of this research work is to improve the

photostability of Si. The effect of WS$_2$ and Au film on the device photostability was examined by tracking the photocurrent densities of Si, WS$_2$/p-Si, and Au-WS$_2$/p-Si photoelectrodes in 0.5 M H$_2$SO$_4$ solution at -1 V for 3000 s. Figure 6b shows the results of the stability tests of the cathodic photocurrent of three samples including Si, WS$_2$/p-Si, and Au-WS$_2$/p-Si photocathode. The photocurrent generated by the bare Si photocathode increased significantly within a short period of time, and the steady state photocurrent became high within few hundreds seconds. The photocurrent density of bare Si increased from ∼−0.17 mA/cm^2 to ∼−0.34 mA/cm^2 (about 2 times higher than the initial photocurrent density) after 3000 s, which can be attributed to the photocorrosion of Si in the electrolyte solution. The corrosion directly leads to the formation of thin SiO$_2$ layer on the surface active sites resulting in increase of surface roughness. Therefore, the resultant increase of the surface roughness and nanostructure enhances the absoprtion and accelerates photoelectrochemical reaction, making good contribution to higher of planar Silicon (see Figure S1). [40] In contrast, after introducing the low cost WS$_2$ film to cover p-Si photocathode, the WS$_2$/p-Si photocathode exhibited almost 1.34 times of the initial photocurrent density of ∼ -0.305 mA/cm^2, indicating that modification of the Si electrode with WS$_2$ film can yield improved photostability in an H$_2$SO$_4$ solution. This suggested that the WS$_2$ film protects p-Si photocathode from photocorrosion and then resulting in facilitating charge separation and transport. Additionally, Figure 6b also shows that the photocurrent density and stability of WS$_2$/p-Si photocathode can be even improved by the coating a layer of Au film, leading to only 1.16 times of the initial photocurrent density of ∼ -0.37 mA/cm^2 after 3000 s test, because the Au film can serve as a good electron acceptor and transporter to conduct charges and suppress the recombination of photogenerated charges effectively. In brief, it is obvious that both WS$_2$ and Au-WS$_2$ passivation layers play a key role in protecting Si photocathode from photochemical corrosion.

4. Conclusion

In conclusion, we have developed a simple and effective strategy to form a heterojunction of Si-WS_2 towards highly efficient and stable photocatalysts. This heterojunction photocathode exhibits higher photocurrent stability and photoactivity compared with the bare Si photocathode. The performance enhancement attributed to the effective physical protection of Si by WS_2, which reduce the photocorrosion during photochemical processes and simultaneously improve the carrier separation and transport of photo-excited charges at WS_2/*p*-Si interface. The optimal photocurrent density was $\sim 1.1 \times 10^{-6}$ A/cm^2 under visible-light illumination about 16 times higher than that of pristine Si photocathode. Moreover, by coating an extra Au film on WS_2/*p*-Si to form Au-WS_2/*p*-Si photocathode, the photocurrent density and stability can also be further improved, revealing the Au film can serve as a good acceptor and conductive layer for electron and further suppress the recombination of photogenerated charges effectively.
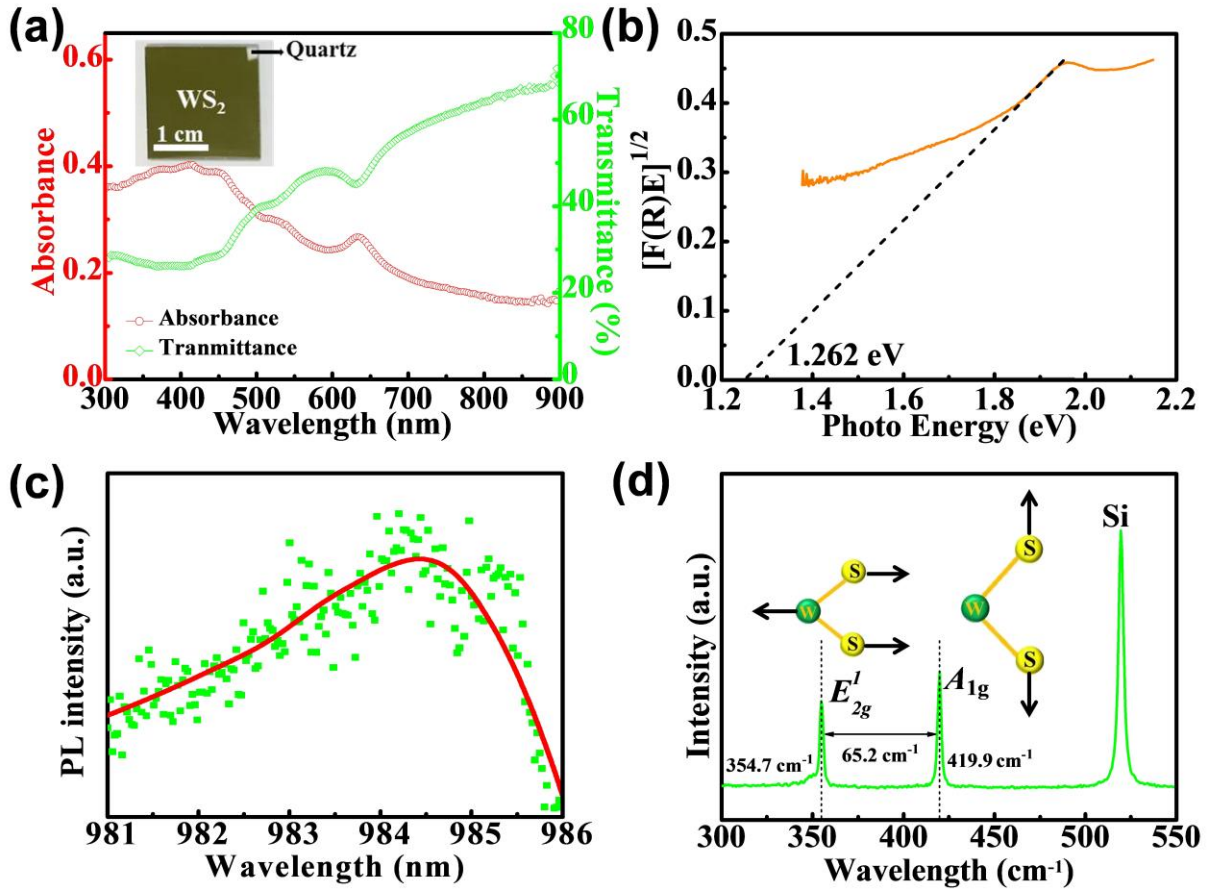
Acknowledgements

Figure 1. (a) Measured UV-visible absorbance and transmittance of the WS$_2$ films. Inset in (a) shows the photograph of an annealed WS$_2$ film on quartz substrate (b) Plot transformed according to the Kubelka-Munk function *versus* photon energy (c) PL spectra of as-synthesized WS$_2$ films. (d) Raman spectrum of the WS$_2$ films on Si substrate. The insets show the illustration of different vibration modes.
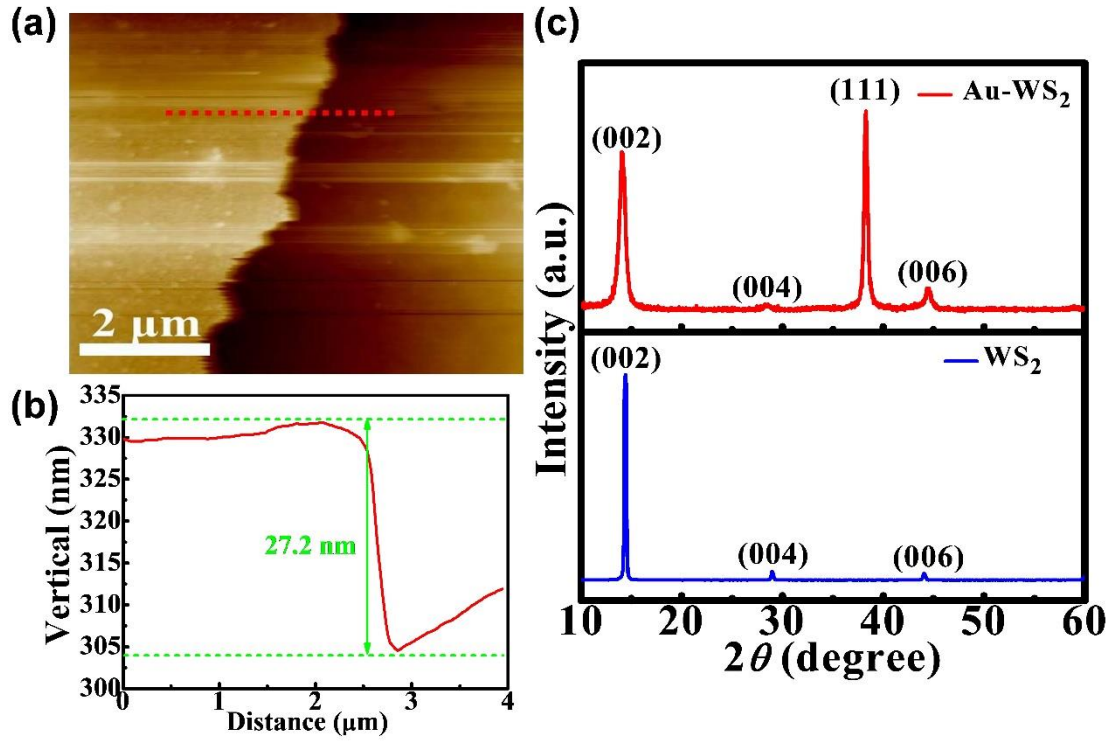
Figure 2. (a) AFM measurements of surface morphology of WS_2 films on SiO_2, the phase image indicating the variation of phase between WS_2 and SiO_2 (b) AFM height profile corresponding to the dotted line shown in (a) indicating a step height of ∼ 27.2 nm. (c) XRD pattern of WS_2 and Au-WS_2.
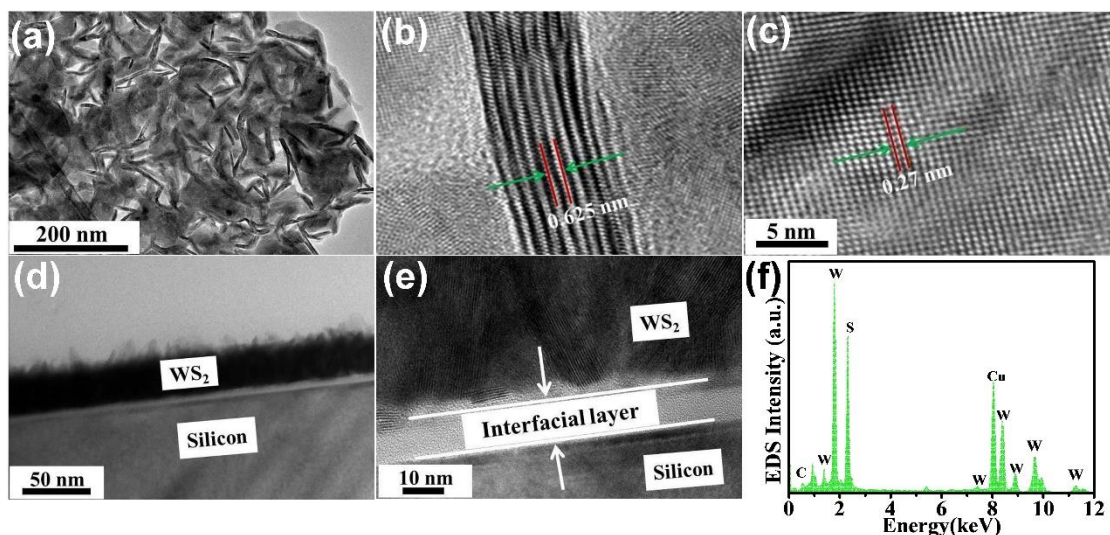
Figure 3. (a) TEM image of transferred WS_2 on the carbon-coated copper fiber. (b) Top-view HRTEM image of the vertically grown WS_2 nanosheets and (c) the horizontally grown WS_2 nanosheets. The lattice spacing are approximately 0.625 and 0.27 nm for vertically and horizontally grown WS_2 nanosheets, respectively. (d) Cross-section TEM image of the heterojunction. (e) HRTEM image of the heterojunction, indicating the existence of an oxidation interfacial layer. (f) EDS spectrum of WS_2 films on the carbon-coated fiber.
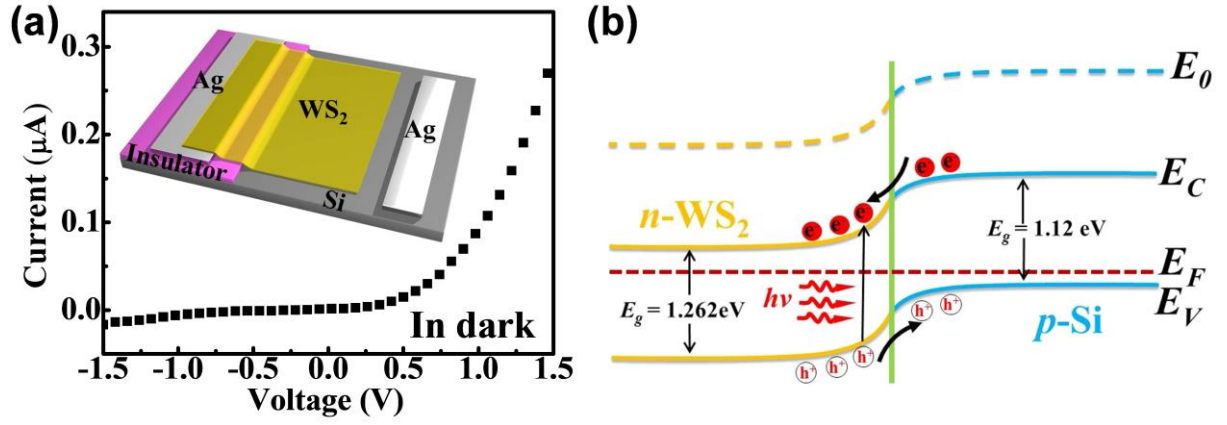
Figure 4. (a) *I-V* characteristic of the WS$_2$/*p*-Si heterojunction measured under dark. (b) Energy band diagram of the WS$_2$/*p*-Si heterojunction under light illumination. The band gap (*E*g) of *p*-Si and *n*-WS$_2$ is 1.12 and 1.262 eV, respectively. *E*$_0$, *E*$_F$, *E*$_C$, and *E*v represent the vacuum energy level, Femi level, bottom of conduction band, and top of the valence band, respectively.
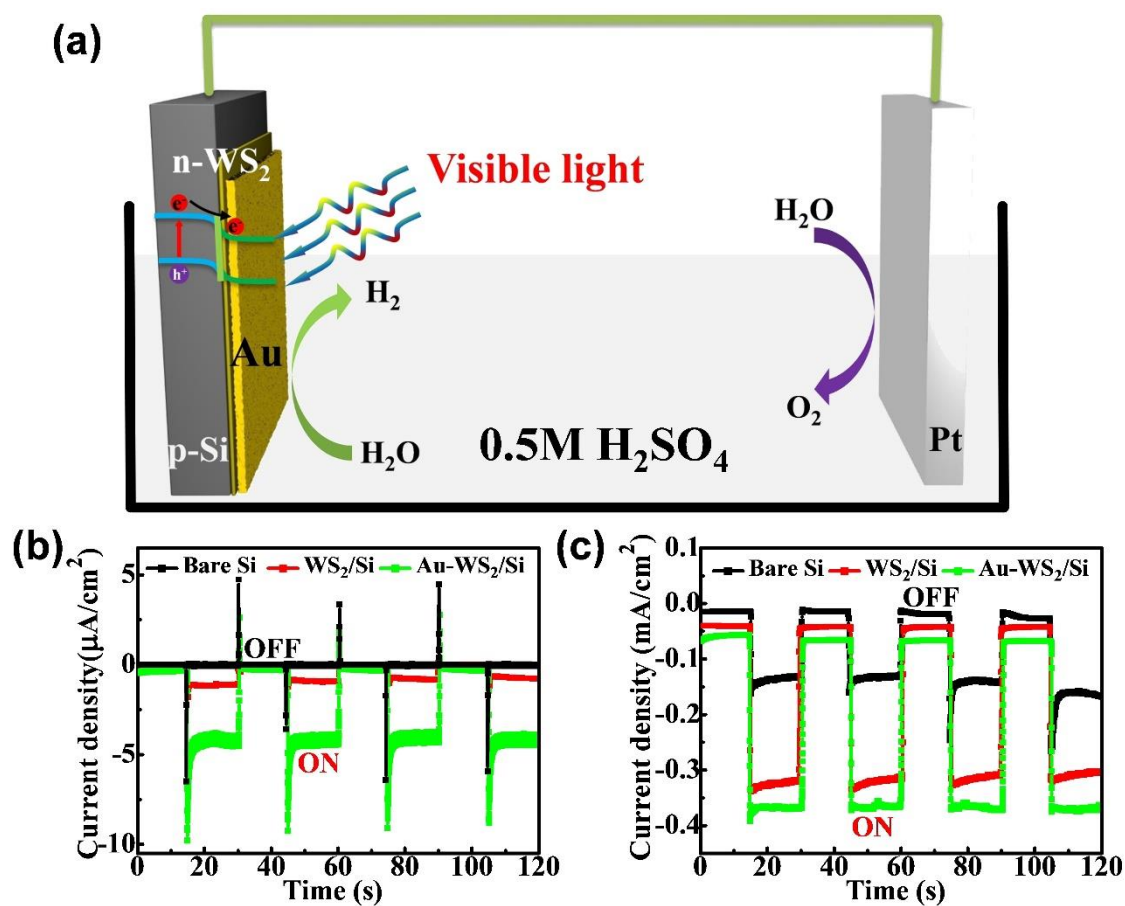
Figure 5. (a) Schematic drawing of the PEC setup. (b) Photocurrent response of Si (black curve), WS$_2$/Si (red curve) and Au-WS$_2$/Si (green curve) at zero voltage *vs*. Ag/AgCl under chopped light illumination. (c) Photocurrent response of bare Si (black curve), WS$_2$/Si (red curve) and Au-WS$_2$/Si (green curve) at the potential of -1 V *vs*. Ag/AgCl under chopped light illumination.
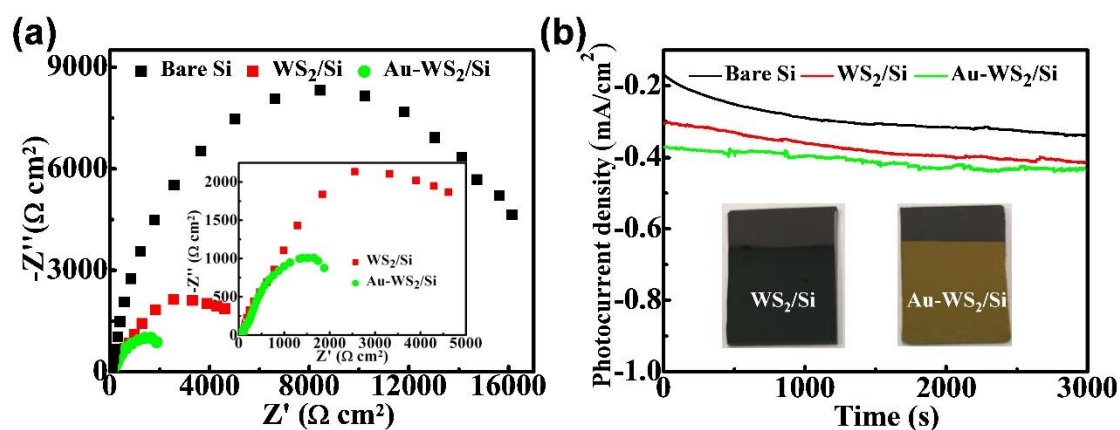
Figure 6. (a) Examples of Nyquist plots of Si electrodes without and with WS_2, Au-WS_2. Measurements were carried out under open-circuit potential and the white light irradiation. (b) Chronoamperometry measurement of photocurrent density of bare Si (black curve), WS_2/p-Si (red curve) and Au-WS_2/p-Si (green curve) photocathodes by using the Pt counter electrode held at a constant potential of -1 V. Inset in (b) shows the photograph of WS_2/p-Si, and Au-WS_2/p-Si photocathodes.

16

Table 1 Comparison of the PEC performances between our Au-WS$_2$/Si heterojunction and other similar sample

Sample	Synthetic method	Maximum Photocurrent	Ref
Au-WS$_2$/Si	Magnetron Sputtering	~ -0.37 mA/cm^2 (-1 V *vs* 0.5 M H$_2$SO$_4$)	Our work
WS$_2$-Au-CIS	CVD growth (Au and CIS incorporated to WS$_2$)	~ 5.2 μA/cm^2 (0 V *vs* 0.5 M Na$_2$SO$_4$)	16
WS$_2$/WO$_3$·H$_2$O	Liquid exfoliation	~ 60 μA/cm^2 (-0.3 V *vs* 1 M H$_2$SO$_4$)	34
Au NP/TiO$_2$-Au film	Spin-coating method (Ti[OCH(CH$_3$)$_2$]$_4$, [HO(CH$_2$)]$_2$NH)	~ 15 μA/cm^2 (0 V *vs* 1 M KOH)	35
rGO-SiNWs	Hummers' method	~ 4 mA/cm^2 (-1.5 V *vs* 0.5 M Na$_2$SO$_4$)	36
P-Si|ZnO(N$_2$)|Ni	Solution based method ((HMTA, Zn(AC)$_2$)	~ 1 mA/cm^2 (-1 V *vs* 0.25 M Na$_2$SO$_4$)	37
TiO$_2$-Au bilayer	ALD deposition	∼12.4 μA/cm^2 (0 V *vs* 1 M KOH)	38

References

1 Y. Cui, M. L. Charles, *Science*, 2001, **291***,* 851-853.

2 L. B. Luo, L. H. Zeng, C. Xie, Y. Q. Yu, F. X. Liang, C. Y. Wu, L. Wang and J. G. Hu, *Sci. Rep.*, 2014**, 4***,* 3914.

3 J. Tang, H. T. Wang, D. H. Lee, M. Fardy, Z. Huo, T. P. Russell, P. D. Yang, *Nano Lett.*, 2010, **10**, 4279-4283.

4 C. Xie, B. Nie, L. H. Zeng, F. X. Liang, M. Z. Wang, L. B. Luo, M. Feng, Y. Q. Yu, C. Y. Wu, Y. C. Wu and S. H. Yu, *ACS Nano*, 2014, **8**, 4015-4022.

5 D. Liu, L. Li, Y. Gao, C. Wang, J. Jiang, Y. J. Xiong, *Angew. Chem. Int. Ed .Engl.*, 2015, **54***,* 2980.

6 J. Oh, T. G. Deutsch, H. C. Yuan, H. M. Branz, *Energy Environ. Sci.*, 2011**, 4***,* 1690-1694.

7 J. Zhou, S. Dai, W. Dong, X. Su, L. Fang, F. Zheng, X. Wang, M. Shen, *Appl. Phys. Lett.*, 2016, **108***,* 213905.

8 L. Zhang, C. Liu, A. B. Wong, J. Resasco, P. D. Yang, *Nano Res.*, 2014*,* **8***,* 281-287.

9 K. Osseo-Asare, D. Wei, K. K. Mishra, *J. Electrochem. Soc.*, 1996*,* **143***,* 749-751.

10 Y. Qu, T. Xue, X. Zhong, Y. C. Lin, L. Liao, J. Choi, X. F. Duan, *Adv. Funct. Mater.*, 2010, **20***,* 3005-3011.

11 B. Mei, B. Seger, T. Pedersen, M. Malizia, O. Hansen, I. Chorkendorff, P. C. Vesborg, *J. Phys. Chem. Lett.*, 2014*,* **5***,*1948-1952.

12 L. L. Tao, H. Long, B. Zhou, S. F. Yu, S. P. Lau, Y. Chai, K. H. Fung, Y. H. Tsang, J. Yao, D. Xu, *Nanoscale*, 2014, **6***,* 9713-9719.

13 L. H. Zeng, L.L. Tao, C. Y. Tang, B. Zhou, H. Long, Y. Chai, S. P. Lau, Y. H. Tsang, *Sci. Rep.* 2016, **6***,* 20343.

14 Y. Yang, H. Fei, G. Ruan, C. Xiang, J. M. Tour, *Adv. Mater.*, 2014, **26***,* 8163-8168.

15 K. C. Kwon, S. Choi, K. Hong, C. W. Moon, Y. S. Shim, D. H. Kim, T. Kim, W. Sohn, J. M. Jeon, C. H. Lee, K. T. Nam, S. Han, S. Y. Kim, H. W. Jang, *Energy Environ. Sci.*, 2016*,* **9***,* 2240-2248

16 Z. Cheng, Z. Wang, T. A. Shifa, F. Wang, X. Zhan, K. Xu, Q. Liu, J. He, *Appl. Phys. Lett.*, 2015, **107***,* 223902.

17 N. Huo, S. Yang, Z. Wei, S. S. Li, J. B. Xia, J. Li, *Sci. Rep.*, 2014, **4***,* 5209.

18 Y. Zhang, Y. F. Zhang, Q. Q. Ji, J. Ju, H. T. Yuan, J.P. Shi, G. Teng, D. L. Ma, M. X. Liu, Y. B. Chen, X. J. Song, H. Y. Hwang, Y. Cui, Z. F. Liu *ACS nano*, 2013,7, 8963-8971.

19 R. K. Chowdhury, R. Maiti, A. Ghorai, A. Midya and S. K. Ray, *Nanoscale*, 2016, **8**, 13429-13436.

20 Y. Sang, Z. Zhao, M. Zhao, P. Hao, Y. Leng, H. Liu, *Adv. Mater.*, 2015, **27**, 363-369.

21 Y. Qi, Q. Xu, Y. Wang, Yan B, Y. Ren, Z. Chen, *ACS Nano*, 2016, **10**, 2903-2909.

22 C. Xu, Y. Liu, B. Huang, H. Li, X. Qin, X. Zhang, Y. Dai, *Appl. Surf. Sci.*, 2011, **257**, 8732-8736.

23 M. Shanmugam, R. Jacobs-Gedrim, E. S. Song, B. Yu, *Nanoscale*, 2014, **6**, 12682-12689.

24 A. Berkdemir, H. R. Gutiérrez, A. R. Botello-Méndez, N. Perea-López, A. L. Elías, C, I, Chia, B, Wang, V. H. Crespi, F. López-Urías, J. C. Charlier, H. Terronesm, M. Terrones, *Sci. Rep.* 2013, **3**, 1775.

25 C. Lan, C. Li, S. Wang, T. He, T. Jiao, D. Wei, W. Jing, L. Li, Y. Liu, *ACS Appl. Mater. Interfaces*, 2016, **8**, 18375-18382.

26 K. Ellmer, *phys. stat. sol. (b)* 2008, **245**, 1745-1760.

27 C. K. Ngaw, V. B. Wang, Z. Liu, Y. Zhou, S. Kjelleberg, Q. Zhang, T. T. Y. Tan, S. C. J. Loo, *npj Biofilms and Microbiomes*, 2015, **1**, 15020.

28 Y. Du, X. Zhu, L. Si, Y. Li, X. Zhou, J. Bao, *J. Phys. Chem. C*, 2015, **119**, 15874-15881.

29 Y. Jung, J. Shen, Y. Liu, J. M. Woods, Y. Sun, J. J. Cha, *Nano Lett.*, 2014, **14**, 6842-6849.

30 C. Liu, D. Kong, P. C. Hsu, H. Yuan, H. W. Lee, Y. Liu, H. Wang, S. Wang, K. Yan, D. Lin, P. A. Maraccini, Parker K M, A, B, Boehm, Y. Cui, *Nat Nanotechnol.*, 2016, DOI: 10.1038/NNANO.2016.138.

31 D. Kong, H. Wang, J. J .Cha, M. Pasta, K. J. Koski, J. Yao, Y. Cui, *Nano Lett.*, 2013, **13**, 1341-1347.

32 Y. Jung, J. Shen, Y. Sun, J. J. Cha, *ACS Nano*, 2014, **8**, 9550-9557.

33 L. H. Zeng, M. Z. Wang, H. Hu, B. Nie, Y. Q. Yu, C. Y. Wu, L. Wang, J. G. Hu, C. Xie, F. X. Liang, L. B. Luo, *ACS Appl. Mater. Interfaces*, 2013, **5**, 9362-9366.

34 P. Zhou, Q. Xu, H. Li, Y. Wang, B. Yan, Y. Zhou, J. Chen, J. Zhang, K. Wang, *Angew. Chem. Int. Ed .Engl.*, 2015, **54**, 15226-30.

35 F. R. Tan, N. Wang, D. Y. Lei, W.Yu, X. M. Zhang, *Adv. Opt. Mater.*, 2017, **5**, 1600399.

36 X. Zhong, G. Wang, B. Papandrea, M. Li, Y. Xu, Y. Chen, C.Y. Chen, H. Zhou, T. Xue, Y. Li, D. Li, Y. Huang, X. Duan, *Nano Res.*, 2015, **8**, 2850-2858.

37 K. Sun, K. Madsen, P. Andersen, W. Bao, Z. Sun, D. Wang, , *Nanotechnology*, 2012, **23**, 194013.

38 F. R. Tan, T. Li, N. Wang, S. K. Lai, C. C. Tsoi, W. Yu, X. M. Zhang, *Sci. Rep.*, 2016, **6**,

33049.

39 Y. Liu, Y. Gu, X. Yan, Z. Kang, S. Lu, Y. Sun, Y. Zhang, *Nano Res.*, 2015, **8**, 2891-2900.

40 S. Li, P. Zhang, X. Song, L. Gao, *ACS Appl. Mater. Interfaces*, 2015, **7**, 18560-18565.